Available online at www.sciencedirect.com

ScienceDirect

Advances in Space Research 62 (2018) 2679–2691

ADVANCES IN SPACE RESEARCH (a COSPAR publication)

www.elsevier.com/locate/asr

Empirical values of branching ratios in the three-body recombination reaction for O(^{1}S) and O_2(0,0) airglow chemistry

Yolián Amaro-Rivera [a,*], Tai-Yin Huang [b], Julio Urbina [a], Fabio Vargas [c]

[a] Department of Electrical Engineering, The Pennsylvania State University, University Park, PA, USA
[b] Department of Physics, The Pennsylvania State University-Lehigh Valley, Center Valley, PA, USA
[c] Department of Electrical Engineering, University of Illinois-Urbana Champaign, IL, USA

Received 28 March 2018; received in revised form 16 July 2018; accepted 18 July 2018
Available online 27 July 2018

Abstract

The branching ratios ε and α in the three-body recombination reaction for O(^{1}S) greenline and O_2(0,0) atmospheric band airglow chemistry represent the fraction of O_2 that branch into the $b^1\sum_g^+$ and $c^1\sum_u^-$ electronic states, respectively. In the present work, the empirical values of these branching ratios have been deduced using a numerical optimization approach. They were obtained using the optimization scheme known as the Covariance Matrix Adaptation Evolution Strategy (CMA-ES) with our MACD-00 model and simultaneous volume emission rate (VER) measurements of the O(^{1}S) greenline and O_2(0,0) atmospheric band emissions. The CMA-ES was employed as the optimization algorithm that would match the O(^{1}S) and O_2(0,0) VER profiles simulated by the MACD-00 model to observations made by OXYGEN/S35, S310.10, NASA Flight 4.339, ETON flights P229H and P230H, OASIS, SOAP/WINE, MULTIFOT, and WINDII. We found that most of the values deduced for ε were in the [0.1, 0.3] range, while most of the values of α were in the [0.01, 0.03] range. Excluding the outliers, the average branching ratio values involving the production of $O_2(b^1\sum_g^+)$ and $O_2(c^1\sum_u^-)$ were determined to be $\varepsilon = 0.15 \pm 0.02$ and $\alpha = 0.018 \pm 0.004$, respectively. Overall, the simulations showed good agreement with the observations albeit with some discrepancies in the peak altitudes and shape of the profiles, possibly due to small perturbations in the observed VER profiles that are not considered in our simulations.

Keywords: O(^{1}S) greenline; O_2 atmospheric band; CMA-ES; Branching ratios; MACD; Airglow; VER

1. Introduction

The O(^{1}S) greenline and O_2 atmospheric band airglow emissions have been broadly studied and provide valuable information on the chemistry and dynamics in the mesosphere and lower thermosphere (MLT) region. Over the years, a number of studies have utilized O(^{1}S) greenline and O_2 atmospheric band observations to derive atomic oxygen densities or to deduce airglow excitation parameters (e.g. McDade et al., 1986; Murtagh et al., 1990; Gobbi et al., 1992; López-González et al., 1992; Melo et al., 1996; Russell and Lowe, 2003, 2004; Gao et al., 2012; Lednyts'kyy et al., 2015). O(^{1}S) greenline and O_2 atmospheric band observations have also been used to characterize dynamical activity in the upper atmosphere and to determine wave parameters (e.g. Taylor et al., 1995; Schubert et al., 1999; Medeiros et al., 2005; Vargas et al., 2015). Thus, accurate knowledge of the chemical reactions and rate coefficients is essential to obtain atomic oxygen densities, to simulate airglow emission profiles and intensities, and to extract wave information from observations.

The branching ratios of multichannel reactions play an important role in both practical applications, i.e. models that involve atmospheric chemistry, and in the understanding of fundamental mechanisms of the chemical reactions

* Corresponding author.
E-mail address: yua120@psu.edu (Y. Amaro-Rivera).

https://doi.org/10.1016/j.asr.2018.07.018
0273-1177/

(Seakins, 2007). The three-body recombination reaction for the O(^{1}S) greenline and O_2 atmospheric bands airglow chemistry consists of:

$$O + O + M \xrightarrow{(1-\varepsilon-\alpha)k_1} O_2 + M \quad (1\text{-R1})$$

$$O + O + M \xrightarrow{\varepsilon k_1} O_2\left(b^1\sum_g^+\right) + M \quad (1\text{-R2})$$

$$O + O + M \xrightarrow{\alpha k_1} O_2\left(c^1\sum_u^-\right) + M \quad (1\text{-R3})$$

where M represents the third-body (major gas species N_2 or O_2), k_1 is the rate coefficient of the three-body recombination reaction, and ε and α are the branching ratios, which represent the fraction of O_2 atoms in the states $O_2(b^1\sum_g^+)$ and $O_2(c^1\sum_u^-)$, respectively. Huang and George (2014) conducted a sensitivity study and found that the branching ratio, α, is the leading determining factor for O(^{1}S) greenline volume emission rate (VER) production whereas the branching ratios, ε and α, determine the O_2(0,0) atmospheric band VER production. Furthermore, they found that the VER of O(^{1}S) greenline decreases with decreasing α and increasing ε, and that the VERs of atmospheric bands increase with increasing ε and decreasing α. The simulated wave-induced secular variations and fluctuations of atmospheric bands also change when different values are assigned to the branching ratios ε and α (Huang and George, 2014). Fig. 1 shows the normalized airglow intensity variation for O_2(0,1) simulated with our MACD-00 model (Amaro-Rivera et al., 2017) using different sets of branching ratios [$\varepsilon = 7 \times 10^{-5}$, $\alpha = 0.04$] and [$\varepsilon = 0.09$, $\alpha = 0.04$]. A gravity wave packet with a forcing wave period of 20-min and horizontal scale of 30-km was used in the simulation to show the effect of an upward propagating gravity wave packet in the O_2 atmospheric band airglow layer. As the figure illustrates, airglow response to a passage of a wave can be very different when different branching ratios are used.

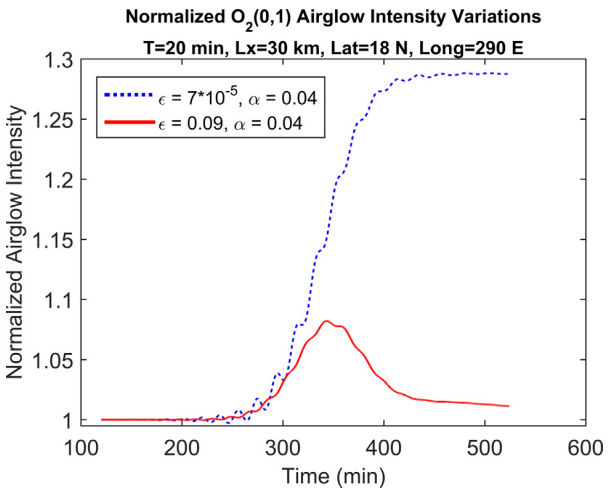

Fig. 1. Time series of wave-induced O_2(0,1) atmospheric band intensity variation when different branching ratios are used in our MACD-00 model.

There is currently a significant discrepancy in the values used for the branching ratios in the three-body recombination reaction. For instance, in their models Hickey et al. (1993) used $\alpha = 0.8$ and $\varepsilon = 0.11$, Snively et al. (2010) used $\alpha = 0.03$ in reaction R3 and did not consider reaction R2 (which involves ε), and Huang and George (2014) used $\alpha = 0.04$ and $\varepsilon = 7 \times 10^{-5}$. Over the years, a number of laboratory or in-situ measurements have been employed to determine these branching ratios. Solheim and Llewellyn (1979) used a O(^{1}S) greenline model and estimated that the fraction of recombination that results in the $O_2(c^1\sum_u^-)$ state was approximately 0.7. Greer et al. (1981) indicated that $\alpha = 0.8$ led to agreement between measured and calculated atmospheric band intensities. Witt et al. (1984) used O_2(0,0) observations from the ETON (Energy Transfer in the Oxygen Nightglow) campaign and determined ε to be in the 0.12–0.2 range. McDade et al. (1986) also used O_2(0,0) atmospheric band VER profiles from the ETON campaign to determine the value of ε. They found that ε was in the range of ~0.02 to ~0.2 and was altitude dependent for direct excitation of $O_2(b^1\sum_g^+)$ in the three-body recombination. Their study suggested that, unless the production of $O_2(b^1\sum_g^+)$ was temperature dependent, direct excitation of $O_2(b^1\sum_g^+)$ in the three-body recombination reaction was not consistent with the O_2(0,0) observations from ETON. Stegman and Murtagh (1991) used observations of the Herzberg I and II bands and deduced that the upper limit for the production efficiency of $O_2(c^1\sum_u^-)$ in the three-body recombination reaction (i.e. branching ratio α) was 0.1. These studies deduced ε or α from observations of a single emission. Our approach considers both O(^{1}S) greenline and O_2(0,0) atmospheric band VER observations, as they occur within a same common volume and involve the same precursor, $O_2(C^1)$ (Huang and George, 2014). The MACD-00 model employed in this study also uses the combined chemical reaction set for O(^{1}S) greenline and O_2(0,0) atmospheric band.

Simultaneously and consecutively measured O(^{1}S) greenline and O_2(0,0) atmospheric band nightglow VER profiles and MACD-00 model simulations were used in this study to deduce the branching ratios ε and α. The different sets of observations were matched to the MACD-00 simulations by employing a numerical optimization approach known as the Covariance Matrix Adaptation Evolution Strategy (CMA-ES).

The paper is organized as follows: Section 2 presents the CMA-ES optimization algorithm employed in our study, Sections 3 and 4 contain a description of the chemistry model and observations, respectively, and Section 5 describes our approach to determine the optimal set of branching ratios based on the MACD-00 model and the observations. Sections 6 and 7 contain the results and

discussion, respectively. The conclusions can be found in section 8.

2. CMA-ES

The CMA-ES (Hansen and Ostermeir, 2001; Hansen et al., 2003) is a powerful, biologically inspired algorithm that performs single-objective real-valued optimization. Some of the advantages of the CMA-ES algorithm include that it can operate on problems that are non-linear, non-quadratic, non-convex, non-separable, and/or ill-conditioned, as well as with large search spaces. Additionally, this self-adaptive algorithm does not require previous knowledge of the optimization problem to be solved and it only needs a few inputs from the user (Gregory et al., 2011 and references therein). The goal with the CMA-ES is to minimize an objective function (cost function) in a continuous domain. The algorithm achieves this by sampling from a Gaussian distribution at each iteration and performing recombination based on the best candidates. The goal is to increase the probability of success in each search step until the optimal solution is found.

The first step in the CMA-ES involves initializing the population parameters (mean m and variance σ) and defining the population size λ . The population is described by a multivariate Gaussian distribution. The algorithm then (1) samples from the population, (2) evaluates the candidates based on an objective (cost) function, and (3) updates parameters. In the third step, the adjusted parameters are the mean vector m, which determines where the next Gaussian search distribution will be centered, the variance σ, which controls the step-size for the algorithm, and the covariance matrix C, which contains information on the shape of the search distribution. The offspring for the next iteration is generated by ranking the evaluated candidates (parents) and performing a weighted recombination using the best candidates μ ($= \lambda/2$). The sample-evaluate-adjust process is repeated until a criterion for the cost function is met or the time expires (Gregory et al., 2015).

The CMA-ES is user-friendly and robust and, under certain conditions, has proven to be faster and more reliable than classical optimization algorithms (Gregory et al., 2015). Thus, we employ the CMA-ES algorithm to find the optimal set of branching ratios ε and α involved in the O(^{1}S) greenline and O_2(0,0) atmospheric band chemistry. In our study, the initial population (λ) consists of 50 random sets of [ε, α] values. Note that each of these branching ratios values represents a fraction so they are limited to the [0,1] range and constrained to $\varepsilon + \alpha \leq 1$. The initial sampling distribution mean (m) and standard deviation (σ) are selected to be half and one-third the value of the branching ratio range, respectively. The branching ratios population is sampled and the MACD-00 simulates the VER profiles for each of the sampled [ε, α] sets. The cost function is

$$c(\varepsilon,\alpha) = \sum_{n\in\{O1S,O2B0\}} |p_{n,obs} - p(\varepsilon,\alpha)_{n,sim}| \quad (1)$$

where $p_{O1S,obs}$ and $p_{O2B0,obs}$ are the O(^{1}S) and the O_2(0,0) peak VER from the observations, respectively, and $p(\varepsilon,\alpha)_{O1S,sim}$ and $p(\varepsilon,\alpha)_{O2B0,sim}$ are the O(^{1}S) and the O_2(0,0) peak VER from the simulation, respectively. The results are ranked and the best values are used by the CMA-ES to adjust and update the mean of the Gaussian search space, as well as its scope and direction for the next iteration. The goal of the CMA-ES algorithm in our study is to constantly self-adapt until the set of branching ratios that produces the lowest cost function is found.

3. Chemistry model

This study utilizes the MACD-00 model, which is a non-linear, time-dependent chemistry dynamics model for the O (^{1}S) greenline and O_2 atmospheric bands airglow. In this study, gravity wave dynamics is set off in the MACD-00 model and so only the chemistry part of the model is used for the simulation. The MACD-00 is based on the work of Huang and George (2014) and is the latest version of MACD model that uses NRLMSISE-00 (Picone et al., 2002) as a reference model of which it outputs atmospheric densities and temperature for a specified date, time, location, AP index, and F10.7 index (Amaro-Rivera et al., 2017). The MACD model has been used over the years in airglow and gravity wave-airglow studies (see Huang and George, 2014; Huang, 2015; 2016; 2017; Amaro-Rivera et al., 2017). The VER for each airglow emission, based on the MACD-00 chemical set, is given by

$$V_{O1S} = \frac{R_{17}R_3R_7[O]^3[M]}{L_4(R_{14}[O_2] + R_{15})} \quad (2)$$

$$V_{O_2(0,1)} = \frac{R_{16}[O]^2[M]}{L_4L_5}\{R_2L_4 + R_3(R_4[O_2] + R_5[N_2] + R_6[O])\} \quad (3)$$

where $L_4 = R_4[O_2] + R_5[N_2] + (R_6 + R_7 + R_8)[O] + R_9$ and $L_5 = R_{10}[N_2] + R_{11}[O_2] + R_{12}[O] + R_{13}$. The rate coefficients R_x can be found in Table 1 of Huang and George (2014), where X corresponds to the number of the chemical reaction listed in the table. The branching ratios ε and α are the subject of study in this paper so their values are determined by the CMA-ES algorithm.

4. O(^{1}S) and O_2(0,0) observations

The dataset used in the present study consists of simultaneous and consecutive measurements of O(^{1}S) greenline and O_2(0,0) atmospheric band emissions. Most of the measurements were obtained with photometers during rocket flight experiments in the 1981–1992 period. These include the OXYGEN/S35 flight (Witt et al., 1984), the S310.10 sounding rocket experiment (Ogawa et al., 1987), the NASA flight 4.339 (Siskind and Sharp, 1991), the ETON P229H rocket flight (Greer et al., 1986), the OASIS

Table 1
VER observations used in the present study.

Source	Date(s)	Latitude, longitude	AP	F10.7	Reference(s)
OXYGEN/S35	February 7, 1981	67.9 N, 21.1 E	20	180.5	Witt et al. (1984)
S310.10	August 24, 1981	31.2 N, 131.1 E	28	258.9	Ogawa et al. (1987)
Flight 4.339	December 7, 1981	32.0 N, 106.0 W	15	287.0	Siskind and Sharp (1991)
ETON P229H	March 23, 1982	57.4 N, 7.4 W	8	202.4	Greer et al. (1986)
ETON P230H	March 23, 1982	57.4 N, 7.4 W	8	202.4	
OASIS	June 11, 1983	32.4 N, 106.3 W	10	139.2	Murtagh et al. (1990)
SOAP/WINE	February 10, 1984	67.9 N, 21.1 E	21	136.7	von Zahn (1987)
MULTIFOT	May 31, 1992	2.3 S, 44.4 W	8	101.8	Takahashi et al. (1996)
WINDII	April 25–26, 1992	~28.0 N, ~312.0 E	9	150.4	G. Shepherd and Y-M. Cho,
WINDII	May 2–3, 1992	~32.0 N, ~313.0 E	11	132.9	private communication, 2017
WINDII	August 27–28, 1992	~21.0 S, ~165.0 W	10	96.7	Liu and Shepherd, 2006

(Oxygen Atom Studies In Space) experiment (Murtagh et al., 1990), the SOAP rocket payload used in the Middle Atmosphere Program/Winter in Northern Europe (MAP/WINE) experiment (von Zahn, 1987), and the MULTIFOT payload onboard the SONDA III rocket (Takahashi et al., 1996). The Wind Imaging Interferometer (WINDII) data were obtained with a Michelson interferometer onboard NASA's Upper Atmosphere Research Satellite (UARS) (Shepherd et al., 1993) and was provided by G. Shepherd and Y-M. Cho (private communication, 2017). The dataset includes a variety of dates, locations, and geophysical conditions. Details for the data, including the references from which the data were obtained, are displayed in Table 1.

In general, most of the O(^{1}S) greenline VER observations used in the present study display a peak between 96 km and 97 km, and most of the O_2(0,0) atmospheric band observations have a peak in the 93 km to 95 km range. Again, because of the diverse atmospheric conditions during each experiment, the peak altitudes, peak VERs, and shape of the profiles vary for each experiment. Details on the instruments, calibration, and data reduction for the observations can be found in (Witt et al., 1984; Ogawa et al., 1987; Siskind and Sharp, 1991; Greer et al., 1986; Murtagh et al. 1990; Takahashi et al., 1996; Shepherd et al., 1993).

5. Methodology

The first step in the process of determining the branching ratios from our MACD-00 model and observations consists of specifying in the model the geophysical conditions (date, time, location, Ap index, and F10.7 index) for when the data were obtained. The MACD-00 model then simulates the VER profiles for an initial set of branching ratios. The CMA-ES algorithm then compares the MACD-00 simulated profile to the measured VER profile. A new population with different sets of branching ratios is determined by the CMA-ES based on the results of the comparison, as described in Section 2. The VER profiles are simulated again using the new set of branching ratios, and the process is repeated until the results converge to an optimal set of values. This process is shown in the flowchart in Fig. 2. An optimal set of branching ratios is determined for each set of measured O(^{1}S) and O_2(0,0) VER profiles independently, following the aforementioned approach.

6. Results

We deduced the branching ratios ε and α for each set of simultaneous or consecutive observations. Figs. 3–13 display the simulated and measured VER profiles for O(^{1}S) greenline and O_2(0,0) atmospheric band. The MACD-00 profiles shown in these figures correspond to the VER values simulated using the optimal set of branching ratios found by the CMA-ES. Tables 2 and 3 show the peak altitudes and peak VERs for O(^{1}S) greenline and O_2(0,0) atmospheric band, respectively. Below are the results for each set of VER observations.

6.1. OXYGEN/S35

Fig. 3 shows the measured and model simulated O(^{1}S) and O_2(0,0) VER profiles from the OXYGEN/S35 campaign. From the figure, we can see there is good agreement between measured and simulated O(^{1}S) VER profiles, particularly above the peak altitude. In the O_2(0,0) case, the measured profile exhibits double peaks present possibly due to wave activity. The upper and lower peaks are located at ~93.82 km and ~88.4 km, respectively. It is interesting to note that the upper peak is at the nominal

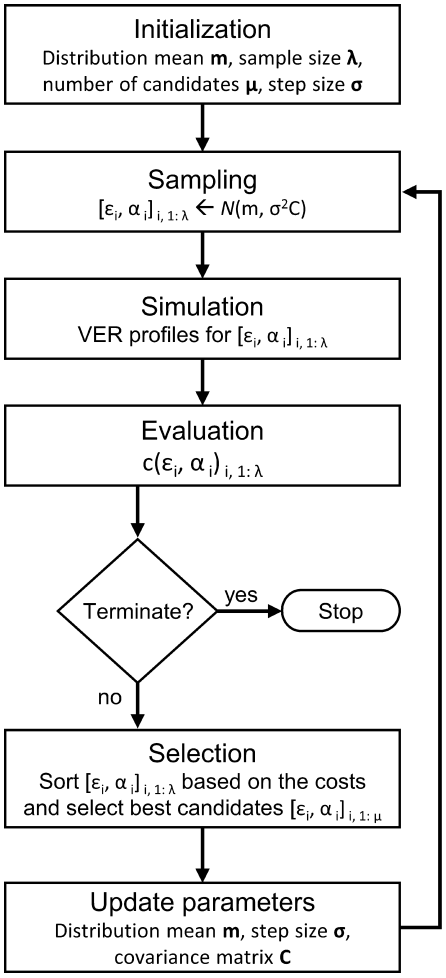

Fig. 2. The flowchart shows the process employed to find the branching ratios.

peak altitude of $O_2(0,0)$ VER and our simulated VER profile had a peak altitude that is closest to the altitude of the upper peak.

6.2. S310.10

Fig. 4 shows the S310.10 measured and model simulated VER profiles for O(^{1}S) greenline and $O_2(0,0)$ atmospheric band. The simulated O(^{1}S) greenline VER profile appears to be lower by ~2 km when compared to the measured profile. The simulated $O_2(0,0)$ profile shows good agreement with the S310.10 measurements, with the S310.10 profile being slightly narrower in the vicinity of the peak.

6.3. Flight 4.339

Fig. 5 shows the measured and model simulated O(^{1}S) and $O_2(0,0)$ VER profiles from Flight 4.339. The measured O(^{1}S) greenline VER profile appears to be disturbed above the peak and is narrower than the simulated profile. Its peak altitude appears to be higher than the simulated peak altitude. The $O_2(0,0)$ measured and simulated profiles show excellent agreement in the peak altitude. The $O_2(0,0)$ VER profile measured on Flight 4.339 is slightly narrower than the simulated profile.

6.4. ETON flights P229H and P230H

Figs. 6 and 7 show the O(^{1}S) greenline and $O_2(0,0)$ VER profiles for ETON flights P229H and P230H, respectively. For each flight, we simulated the VER profiles using atomic oxygen densities ([O]) from NRLMSISE-00 and using [O] observations from the ETON campaign (Greer et al., 1986). In general, our MACD-00 simulated VER profiles exhibited excellent agreement with the ETON measured VER profiles. For the ETON P229H case, the measured O(^{1}S) greenline VER profile displays a 0.49 km difference in the peak altitude when compared to the simulation that uses [O] from NRLMSISE-00 and a 1.11 km difference when compared to the simulation that uses [O] from ETON. The peak altitude difference in the $O_2(0,0)$ profiles is 0.4 km when comparing the measured VER

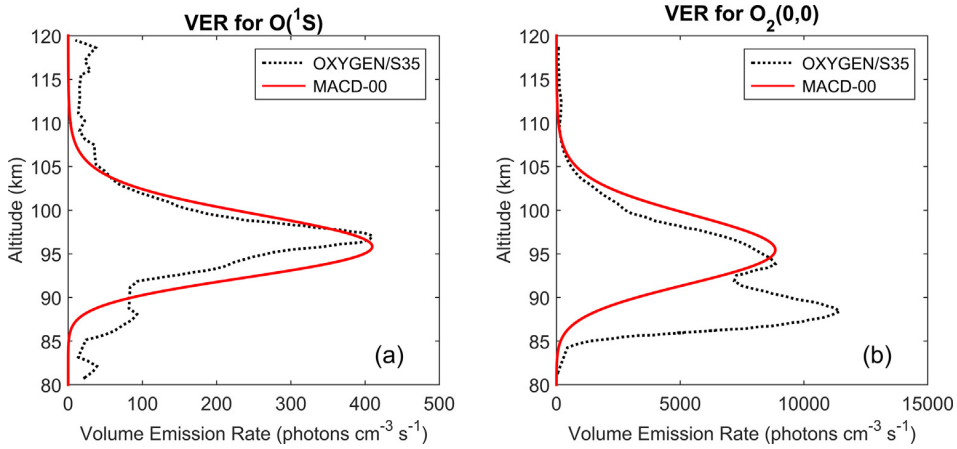

Fig. 3. Model simulated and OXYGEN measured VER profiles for (a) O(^{1}S) and (b) $O_2(0,0)$.

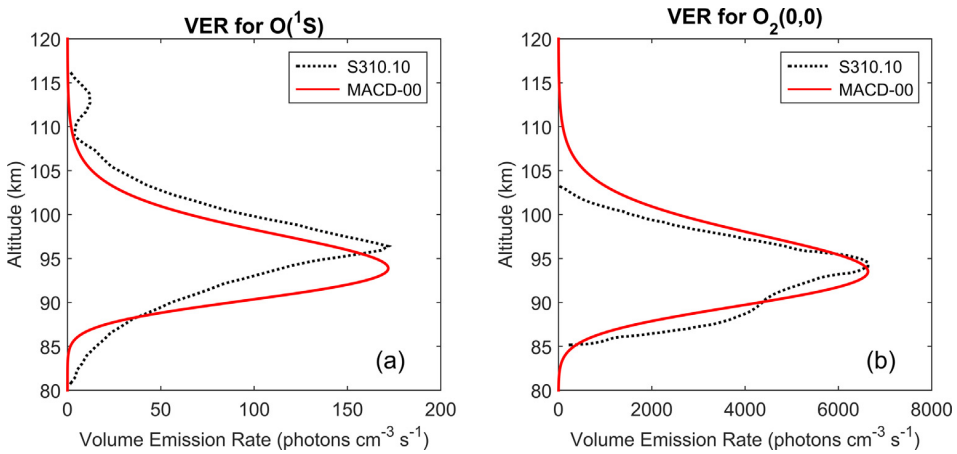

Fig. 4. Model simulated and S310.10 measured VER profiles for (a) O(^{1}S) and (b) O_2(0,0).

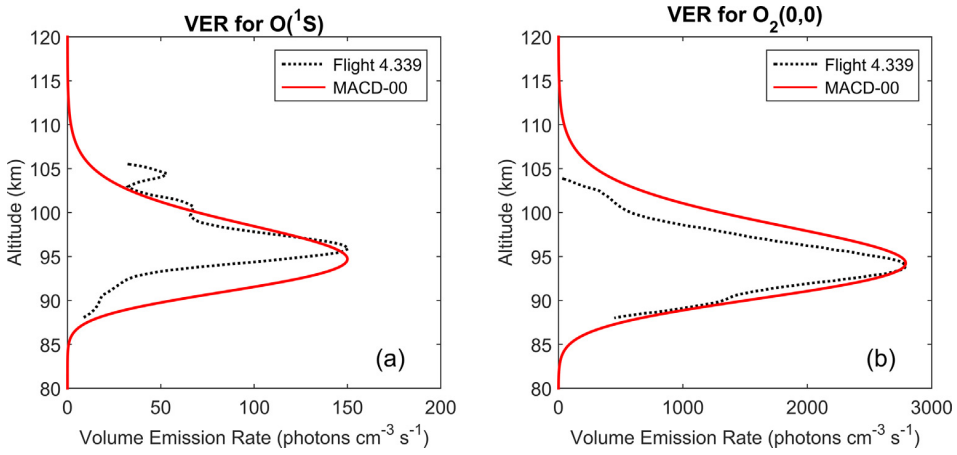

Fig. 5. Model simulated and Flight 4.339 measured VER profiles for (a) O(^{1}S) and (b) O_2(0,0).

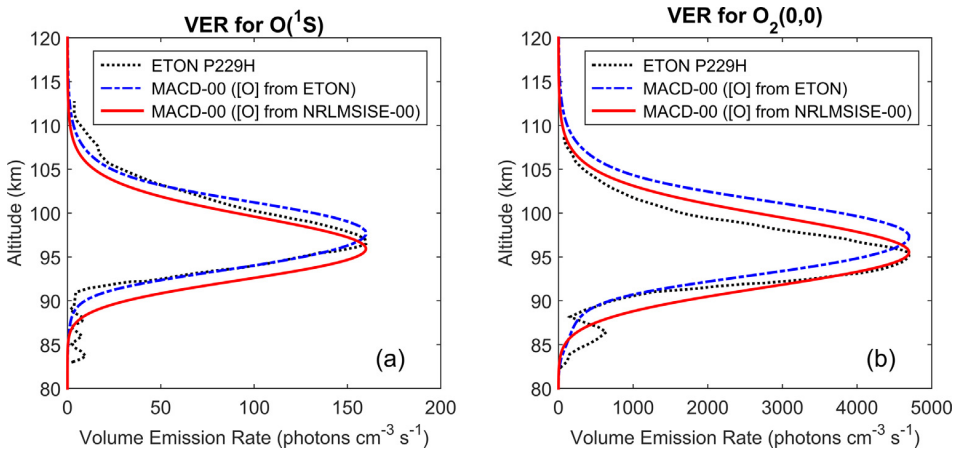

Fig. 6. Model simulated and ETON P229H measured VER profiles for (a) O(^{1}S) and (b) O_2(0,0).

profile to the simulation that uses [O] from NRLMSISE-00, and 2.3 km when comparing the measured VER profile to the simulation that uses [O] from ETON.

The ETON P230H O(^{1}S) greenline results show that the simulation that uses [O] from NRLMSISE-00 is lower by ~2 km compared to the measurements, while

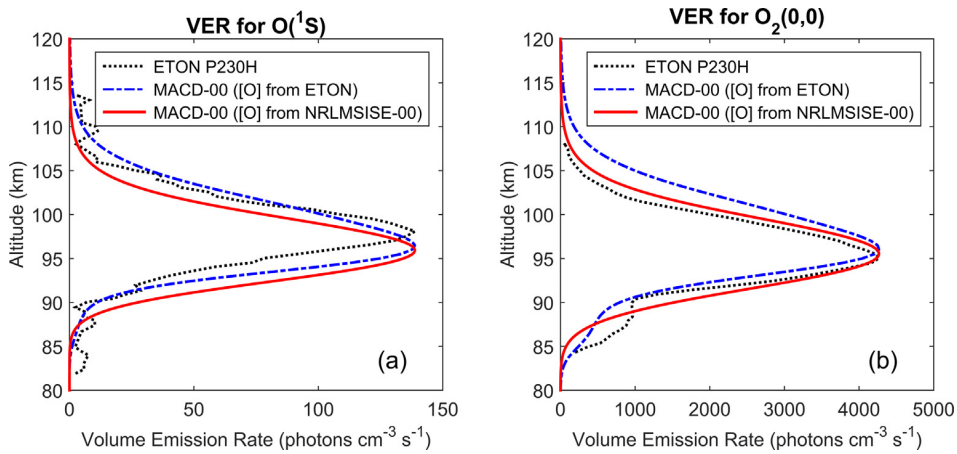

Fig. 7. Model simulated and ETON P230H measured VER profiles for (a) O(^{1}S) and (b) O_2(0,0).

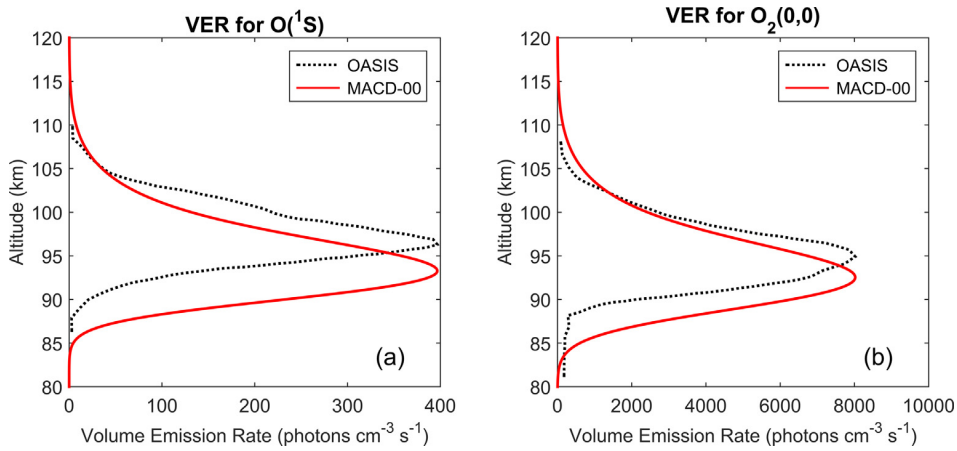

Fig. 8. Model simulated and OASIS measured VER profiles for (a) O(^{1}S) and (b) O_2(0,0).

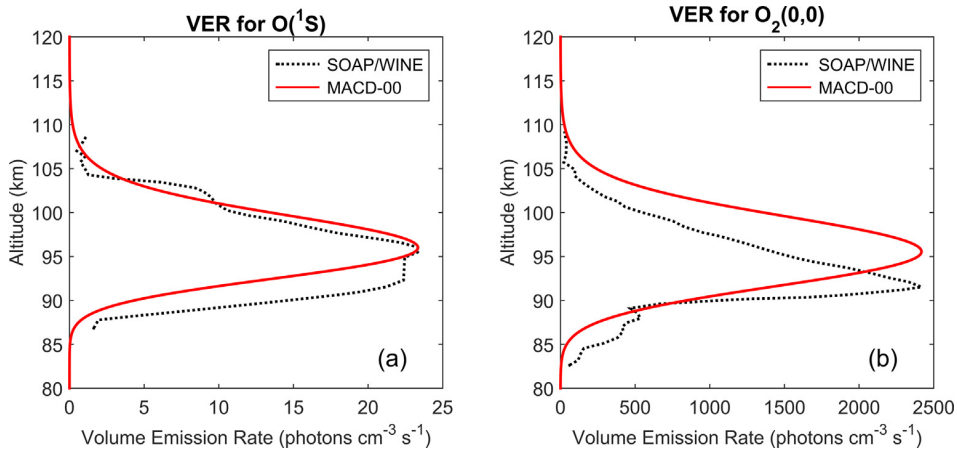

Fig. 9. Model simulated and SOAP/WINE measured VER profiles for (a) O(^{1}S) and (b) O_2(0,0).

the simulation that uses [O] from ETON produces a VER profile that is ~1.6 km higher. The ETON P230H O_2(0,0) profiles display excellent agreement in the shape and only a 0.48 km and a 0.98 km difference in the peak altitude when comparing the VER measurements to the simulation that uses [O] from NRLMSISE-00 and to the simulation that uses [O] from ETON, respectively.

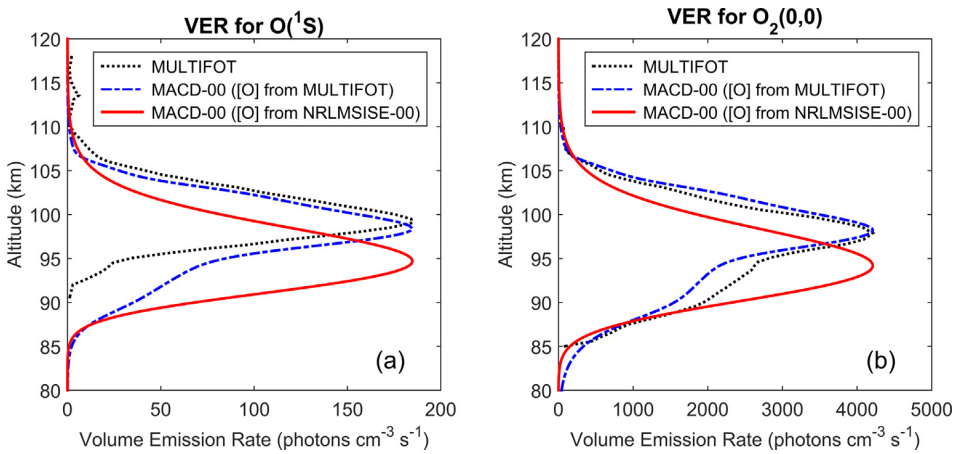

Fig. 10. Model simulated and MULTIFOT measured VER profiles for (a) O(^{1}S) and (b) O_2(0,0).

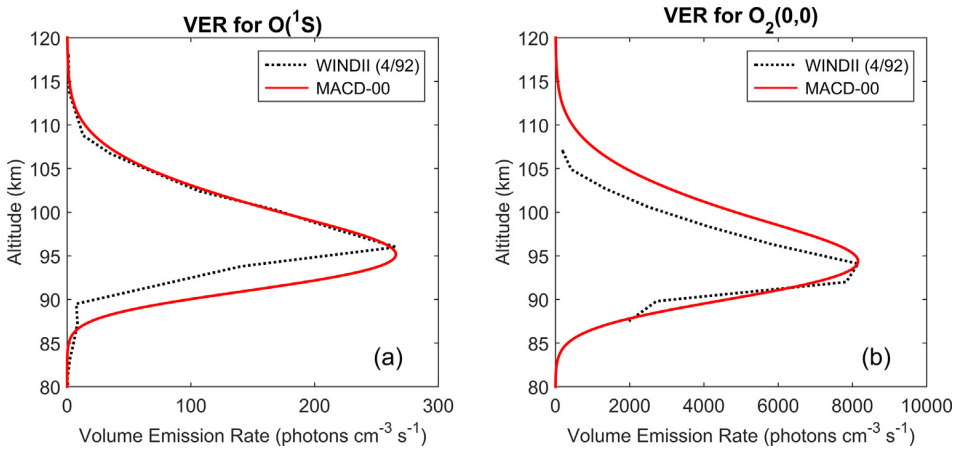

Fig. 11. Model simulated and WINDII (4/92) measured VER profiles for (a) O(^{1}S) and (b) O_2(0,0).

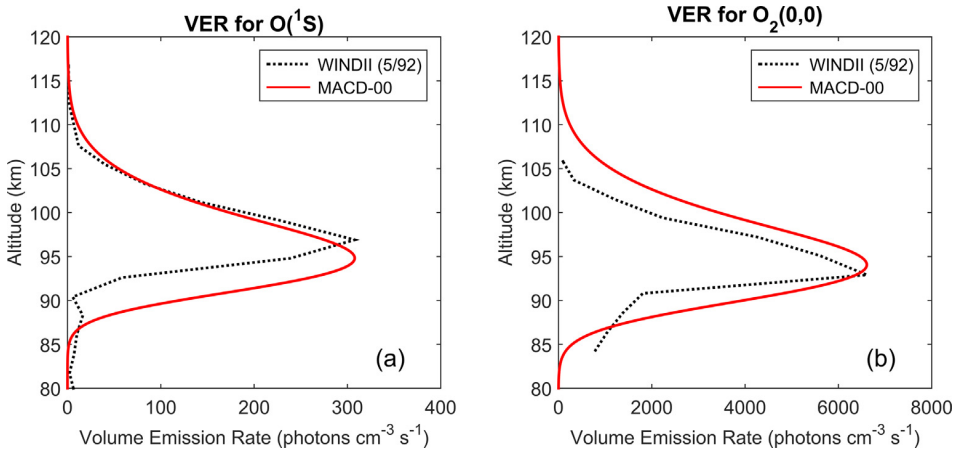

Fig. 12. Model simulated and WINDII (5/92) measured VER profiles for (a) O(^{1}S) and (b) O_2(0,0).

6.5. OASIS

Fig. 8 shows the model simulated and OASIS measured O(^{1}S) and O_2(0,0) VER profiles. The simulated O(^{1}S) greenline and O_2(0,0) atmospheric band VER profiles both appear to be lower by $\sim$3 km when compared to the OASIS measurements but in general display good agreement in terms of the shape.

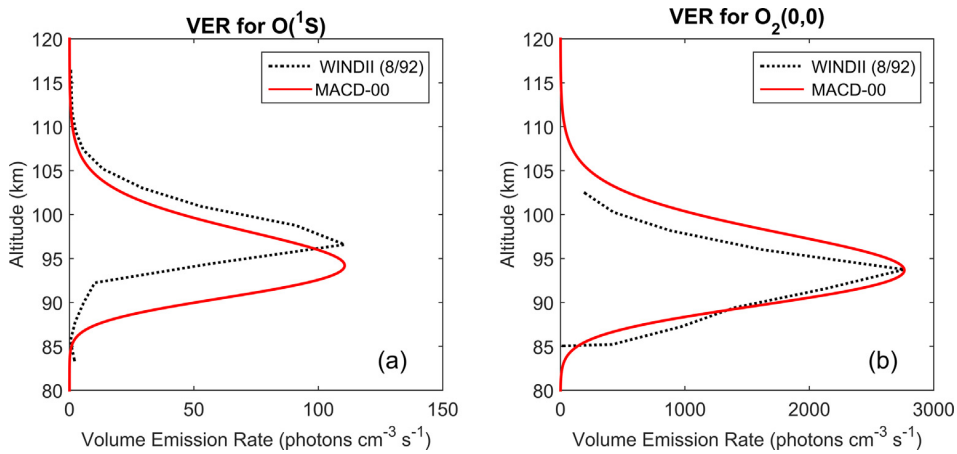

Fig. 13. Model simulated and WINDII (8/92) measured VER profiles for (a) O(^{1}S) and (b) O_2(0,0).

Table 2
Peak VER and altitude for O(^{1}S) greenline measured and simulated profiles.

Source	Peak VER (photons cm^{-3} s^{-1})	Altitude (km)		
		Measured	Simulated	Difference
OXYGEN/S35	409.6	97.08	95.9	1.18
S310.10	171.9	96.39	93.9	2.49
Flight 4.339	150.5	95.87	94.8	1.07
ETON P229H	159.9	96.49	96.0	0.49
ETON P229H ([O] from ETON)			97.6	1.11
ETON P230H	138.8	98.09	96.0	2.09
ETON P230H ([O] from ETON)			96.5	1.59
OASIS	396.7	96.29	93.3	2.99
SOAP/WINE	23.34	96.04	96.0	0.04
MULTIFOT	184.8	99.06	94.7	4.36
MULTIFOT ([O] from MULTIFOT)			98.4	0.66
WINDII (4/92)	265.7	96.0	95.2	0.8
WINDII (5/92)	307.8	96.9	94.8	2.1
WINDII (8/92)	110.6	96.6	94.3	2.3

Table 3
Peak VER and altitude for O_2(0,0) atmospheric band measured and simulated profiles.

Source	Peak VER (photons cm^{-3} s^{-1})	Altitude (km)		
		Measured	Simulated	Difference
OXYGEN/S35	$1.144 \times 10^{4*}$	88.4*	95.4	7.0
	8843**	93.82**		1.58
S310.10	6634	94.55	93.5	1.05
Flight 4.339	2791	93.98	94.2	0.22
ETON P229H	4696	95.1	95.5	0.4
ETON P229H ([O] from ETON)			97.4	2.3
ETON P230H	4266	95.02	95.5	0.48
ETON P230H ([O] from ETON)			96.0	0.98
OASIS	8022	94.91	92.5	2.41
SOAP/WINE	2418	91.53	95.5	3.97
MULTIFOT	4210	97.89	94.2	3.69
MULTIFOT ([O] from MULTIFOT)			98.2	0.31
WINDII (4/92)	8152	94.1	94.4	0.3
WINDII (5/92)	6609	92.9	94.0	1.1
WINDII (8/92)	2763	93.75	93.7	0.05

* Lower.
** Upper.

6.6. SOAP/WINE

Fig. 9 contains the O(^{1}S) and O_2(0,0) VER profiles from model simulations and measurements for SOAP/WINE. The O(^{1}S) VER profiles display excellent agreement in the peak altitude with only a 0.04 km difference. We note that the measured O(^{1}S) VER between 92 km and 95 km appears to be the same, which is peculiar and so we are not sure if they were real. The O(^{1}S) VER profile obtained during the SOAP/WINE campaign displays larger VER values below the peak altitude than the MACD-00 simulated profile. The simulated and measured O_2(0,0) VER profiles display a ~4 km difference in the peak altitude. The SOAP/WINE measurements exhibit a peak lower than the nominal peak altitude and the profile appears to be displaced downward compared to the profile obtained from simulations.

6.7. MULTIFOT

Fig. 10 displays the MULTIFOT measured and model simulated O(^{1}S) and O_2(0,0) VER profiles. The VER profiles were simulated using [O] from NRLMSISE-00 and with [O] obtained from the O_2(0,0) atmospheric band emission measured in the MULTIFOT rocket experiment (Melo et al., 1996). For both O(^{1}S) greenline and O_2(0,0) atmospheric band, the VER profiles simulated using [O] from NRLMSISE-00 appear to be lower by ~4 km when compared to the MULTIFOT VER measurements. The whole MULTIFOT profiles appear to be moved upwards, given that the peak altitudes in the measured profiles are higher than the nominal peak altitudes. The VER profiles simulated using [O] from MULTIFOT are in good agreement with the MULTIFOT measured VERs with only a 0.66 km between the O(^{1}S) VER profiles and a 0.31 km difference between the O_2(0,0) VER profiles. This is not surprising given that the [O] profile was derived from the MULTIFOT measured O_2(0,0) emission.

6.8. WINDII

Figs. 11–13 show O(^{1}S) and O_2(0,0) VER profiles obtained from our MACD-00 model and measured with the WINDII instrument. Fig. 11 shows the VER profiles obtained for April 25–26, 1992. For the O(^{1}S) greenline emission, there was excellent agreement between the simulation results and the measurements above the peak altitude. The peaks display a 0.8 km difference in altitude. Below the peak altitude, the simulated profile displays larger values than the measured values. On the other hand, the O_2(0,0) profiles display excellent agreement below the peak altitude, while the model presents larger values above the peak. There is excellent agreement in the peak altitude, with only a 0.3 km difference between the peaks. The measured VER profiles both were narrower (smaller half-width maximum) than the model simulations.

Table 4
Deduced branching ratios.

Source	ε	α
OXYGEN/S35	0.4413	0.0708
S310.10	0.2197	0.0183
Flight 4.339	0.0310	0.0045
ETON P229H	0.1371	0.0150
ETON P229H ([O] from ETON)	0.1169	0.0117
ETON P230H	0.1247	0.0130
ETON P230H ([O] from ETON)	0.1432	0.0151
OASIS	0.6205	0.1328
SOAP/WINE	0.1534	0.0055
MULTIFOT	0.1070	0.0153
MULTIFOT ([O] from MULTIFOT)	0.1094	0.0138
WINDII (4/92)	0.3213	0.0378
WINDII (5/92)	0.2857	0.0500
WINDII (8/92)	0.0985	0.0136

Fig. 12 shows the model simulated and WINDII measured VER profiles for May 2–3, 1992. The simulated and measured O(^{1}S) greenline VER profiles display a ~ 2 km difference in their peak altitudes while the O_2(0,0) profiles display a ~ 1 km difference. The model simulated and WINDII measured O(^{1}S) greenline VER profiles display excellent agreement above the peak altitude, while the profile obtained from simulation shows larger values below the peak.

Fig. 13 shows the model simulated and WINDII measured VER profiles for August 27–28, 1992. The peaks in the O(^{1}S) greenline VER profiles display a ~2 km difference in altitude, while the simulated and measured O_2(0,0) VER peaks are separated by only 0.05 km. The simulated O(^{1}S) greenline VER profile is lower by ~1 km and has larger values than the measured profile below the peak altitude. The simulated O_2(0,0) VER profile shows larger values than the measured values above the peak altitude. Note that most of the simulated VER profiles seem to have a larger half-width maximum than the measured VER profiles.

All of the branching ratios were computed independently for each set of simultaneous or consecutive observations and can be found in Table 4. The range of the branching ratios for ε is between 0.0985 and 0.6205, and for α it is between 0.0055 and 0.1328. The average branching ratios, after excluding the outliers (OXYGEN/S3 and OASIS), are $\varepsilon = 0.15 \pm 0.02$ and $\alpha = 0.018 \pm 0.004$.

7. Discussion

As previously mentioned, α is the leading determining factor for the O(^{1}S) greenline VER production, whereas the branching ratios ε and α determine the O_2(0,0) atmospheric band VER production (Huang and George, 2014). We have done a similar sensitivity study and the results are shown in Figs. 14–16. Fig. 14 illustrates the effect on the O_2(0,0) VER profile when $\alpha = 0.018$ and

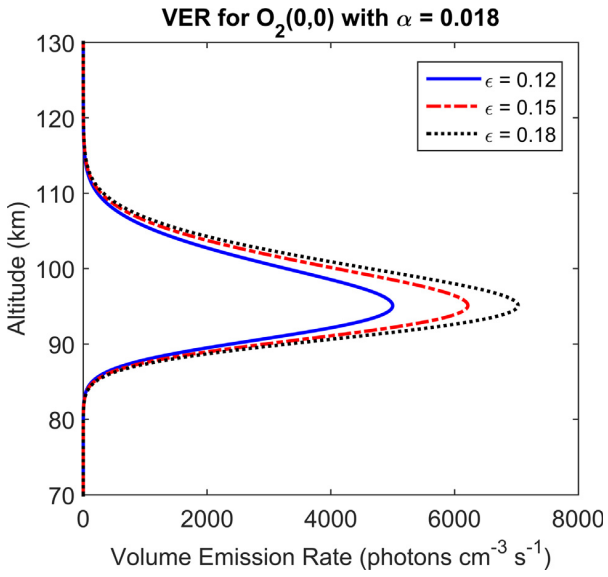

Fig. 14. Simulated $O_2(0,0)$ VER when $\alpha = 0.018$ and different values of ε are used in our MACD-00 model.

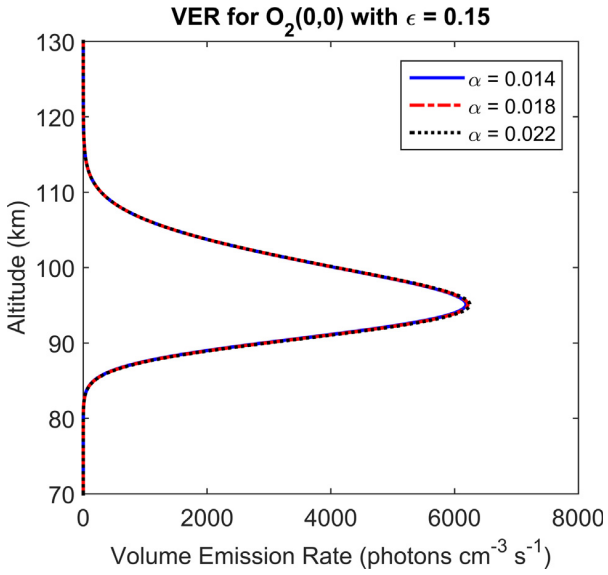

Fig. 15. Simulated $O_2(0,0)$ VER when $\varepsilon = 0.15$ and different values of α are used in our MACD-00 model.

different values of ε are used. Changing ε from 0.12 to 0.15 changes the $O_2(0,0)$ peak VER from 4999 photons cm^{-3} s^{-1} at 95.1 km to 6214 photons cm^{-3} s^{-1} at 95.1 km. Fig. 15 shows $O_2(0,0)$ VER profiles when $\varepsilon = 0.15$ and different values of α are used. In this case the peak VER goes from 6184 photons cm^{-3} s^{-1} at 95.1 km to 6214 photons cm^{-3} s^{-1} at 95.1 km for $\alpha = 0.014$ and $\alpha = 0.018$, respectively. As these two figures show, the branching ratio ε has a greater impact on the $O_2(0,0)$ VER production than α. The $O(^1S)$ greenline VER is not affected by the branching ratio ε (figure not shown), while the branching ratio α

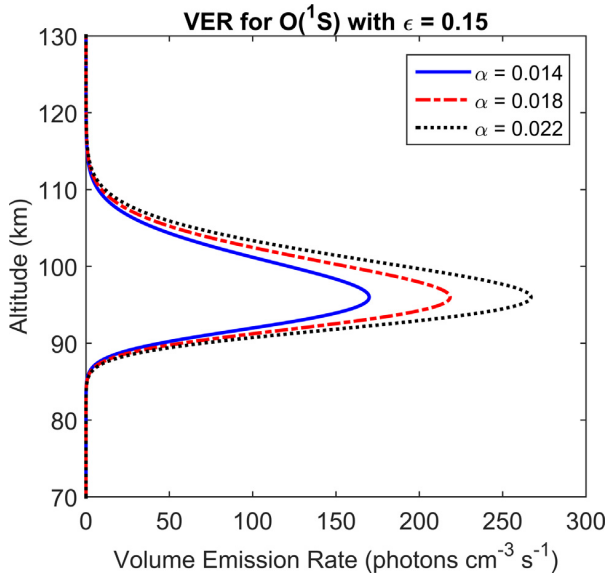

Fig. 16. Simulated $O(^1S)$ VER when $\varepsilon = 0.15$ and different values of α are used in our MACD-00 model.

changes the peak value of the VER profile from 169.9 photons cm^{-3} s^{-1} at 96.0 km to 218.5 photons cm^{-3} s^{-1} at 96.0 km, as seen in Fig. 16. Our sensitivity study illustrates that the $O_2(0,0)$ peak VER increases with increasing ε and with increasing α, and the $O(^1S)$ peak VER increases with increasing α. It is important to mention that the branching ratios values used for the sensitivity study (Figs. 14–16) were chosen based on the averages and standard deviations obtained from our numerical optimization approach. Based on that, the VER profiles are not seen to change much in Fig. 15, however, there is a small increase of $O_2(0,0)$ VER with increasing α. Fig. 15 also seems to suggest that it is ε that is the leading factor in determining the $O_2(0,0)$ production.

The present study is based on 11 sets of simultaneous or consecutive VER measurements of $O(^1S)$ greenline and $O_2(0,0)$ atmospheric band. The CMA-ES optimization algorithm was utilized to match the peak VERs from our MACD-00 model simulation to the peak VERs from measured VER profiles to deduce the branching ratios ε and α. Most of the simulated VER profiles displayed good agreement with the observations. Except for the SOAP/WINE case, the $O(^1S)$ greenline VER profiles obtained from our MACD-00 model display a peak at a lower altitude than the measurements. For $O_2(0,0)$, most of the peaks of the simulated VER profiles were in excellent agreement with peak altitudes of the observations. That being said, in general, OXYGEN/S35 presented a large difference between measurements and simulation in terms of the shape of the $O(^1S)$ greenline and $O_2(0,0)$ VER profiles. As explained by Murtagh et al. (1990), these measurements were obtained from high-latitudes during sudden stratospheric warming events, so it is possible that the NRLMSISE-00 reference model does not capture this well. This might

reflect in the branching ratios deduced from these observations. The branching ratio ε deduced from OXYGEN/S35 was large compared to the values determined from the other sets of measurements. We also note that the branching ratio ε, 0.6205, obtained from the OASIS measurements was the largest of all the values.

We have also considered the effect of the Ap and F10.7 indices on the O(^{1}S) and O_2(0,0) VER profiles in order to better understand if they play a role in the difference in peak altitudes between simulations and measurements. The present study uses a daily average Ap index as a proxy for geomagnetic activity. It has been shown that the F10.7 index does not seem to change the airglow VER peak altitudes but the Ap index does (Huang, 2017), so we do not expect F10.7 to be a factor in the VER peak altitude difference. We did a sensitivity study with the OXYGEN/S35 data as they were obtained on a date when a large Ap variation (from 2 nT to 80 nT) was present. From our simulation we found that if Ap = 2 nT is used, there would be a 0.3 km difference in the simulated O(^{1}S) VER peak altitude and a 0.2 km difference in the simulated O_2(0,0) VER peak altitude when compared to the value Ap = 20 nT adopted in this study. Using Ap = 80 nT, there would be a 0.2-km difference in the simulated O(^{1}S) VER peak altitude and a 0.3-km difference in the simulated O_2(0,0) VER peak altitude when compared to the value used in this study. This suggests that the selection of the Ap value could have a small impact on the simulated VER peak altitude in some cases like the one discussed above. The airglow VER peak altitudes mainly depend on the major gas species densities and temperature (Huang, 2017), which in this study are obtained from the NRLMSISE-00 empirical model. The [O] number density seems to play a role in the airglow VER peak altitude. This can be seen in Fig. 10, where the O(^{1}S) and O_2(0,0) VER profiles are simulated with different [O] initial profiles. The simulations that use [O] obtained from the MULTIFOT measured O_2(0,0) emission lead to VER profiles that are closest to the MULTIFOT VER measurements, while the O(^{1}S) and O_2(0,0) VER simulations with [O] from NRLMSISE-00 are ~4 km lower than the MULTIFOT VER measurements.

It is also important to note that NRLMSISE-00 outputs temporally averaged data, so gravity wave-induced variations are not expected in our simulation results. This can be seen in some of the figures, where the measured profiles contain wave-like variations. That being said, more simultaneous measurements of the O(^{1}S) greenline and O_2(0,0) atmospheric band emissions during low-wave activity conditions are needed to better categorize the branching ratios during quiet-time period. More data is also necessary to investigate if the values of the branching ratios depend on location or season. Nonetheless, in the present study we used a limited number of observations obtained from different locations and different seasons, and found that most of the values deduced for ε were in the [0.1, 0.3] range, while most of the values of α were in the [0.01, 0.03] range.

8. Conclusions

We have presented a numerical optimization approach to deducing the branching ratios ε and α of the three-body recombination reaction for O(^{1}S) greenline and O_2 atmospheric bands airglow chemistry. The CMA-ES algorithm was employed as the optimization scheme that would match the O(^{1}S) and O_2(0,0) VER profiles simulated by the MACD-00 model to observations made by OXYGEN/S35, S310.10, NASA Flight 4.339, ETON flights P229H and P230H, OASIS, SOAP/WINE, MULTIFOT, and WINDII. The observations used in the present study consist of simultaneous or consecutive VER measurements of O(^{1}S) greenline and O_2(0,0) atmospheric band. Our simulation results show good agreement with the observations.

From our study, the average branching ratio values involving the production of $O_2(b^1\sum_g^+)$ and $O_2(c^1\sum_u^-)$ were determined to be $\varepsilon = 0.15 \pm 0.02$ and $\alpha = 0.018 \pm 0.004$, respectively. The calculation for the averages did not include the outliers, OXYGEN/S35 and OASIS, as the branching ratios deduced from those observations greatly differ from the others, possibly due to the presence of wave activity in those profiles. Our study also shows that ε and α bear a linear relationship described by $\alpha = 0.2096\varepsilon - 0.0138$ ($R^2 = 0.9237$). This relationship was established by applying a linear fit to the values found for ε and α.

The present study highlights the necessity of simultaneous measurements of O(^{1}S) greenline and O_2(0,0) atmospheric band at different locations and seasons during low-wave activity conditions. Our work also elucidates the need for modelling studies of O(^{1}S) greenline and O_2 atmospheric bands airglow emissions in the MLT region. This is essential, as understanding the airglow chemistry and rate coefficients involved in airglow emissions is crucial for accurately extracting dynamic features like wave characteristics or inferring [O] density profiles from airglow observations. We are currently in plans of expanding our study to include O(^{1}S) greenline and O_2(0,0) atmospheric band data obtained with the SCIAMACHY spectrometer on the Envisat satellite (Christian von Savigny and Miriam Sinhuber, private communications, 2017), as well as airglow observations from the Andes Lidar Observatory (ALO) in Chile, to better understand if the branching ratios depend on location, season, or atmospheric conditions.

Acknowledgements

Y. Amaro-Rivera would like to thank the Alfred Sloan Foundation for providing financial support. We thank G. Shepherd and Y-M. Cho for providing WINDII data for our study. This study used the NRLMSISE-00 model (Picone et al. 2002) from the CEDAR Database at the National Center for Atmospheric Research, which is supported by the National Science Foundation of the United States of America.

References

Amaro-Rivera, Y., Huang, T.-Y., Urbina, J., 2017. On the importance of an atmospheric reference model: a case study on gravity wave-airglow interactions. J. Atmos. Sol. Terr. Phys. https://doi.org/10.1016/j.jastp.2017.08.020 (in press).

Gao, H., Nee, J.-B., Xu, J., 2012. The emission of oxygen green line and density of O atom determined by using ISUAL and SABER measurements. Ann. Geophys. 30, 695–701. https://doi.org/10.5194/angeo-30-695-2012.

Gobbi, D., Takahashi, H., Clemesha, B., Batista, P., 1992. Equatorial atomic oxygen profiles derived from rocket observations of OI 557.7 nm airglow emission. Planet. Space Sci. 40, 775–781.

Greer, R.G.H., Llewellyn, E.J., Solheim, B.H., Witt, G., 1981. The excitation of O2(b1) in the nightglow. Planet. Space Sci. 29 (4), 383–389. https://doi.org/10.1016/0032-0633(81)90081-7, ISSN 0032-0633.

Greer, R.G.H., Murtagh, D.P., McDade, I.C., Dickinson, P.H.G., Thomas, L., Jenkins, D.B., Stegman, J., Llewellyn, E.J., Witt, G., Mackinnon, D.J., Williams, E.R., 1986. ETON1—a database pertinent to the study of energy-transfer in the oxygen nightglow. Planet. Space Sci. 34 (9), 771–788.

Gregory, M.D., Werner, D.H., 2011. Next generation electromagnetic optimization with the covariance matrix adaptation evolutionary strategy. In: 2011 IEEE International Symposium on Antennas and Propagation (APSURSI), Spokane, WA, pp. 2423–2426.

Gregory, M.D., Martin, S.V., Werner, D.H., 2015. Improved electromagnetics optimization: the covariance matrix adaptation evolutionary strategy. IEEE Antennas Propag. Mag. 57 (3), 48–59. https://doi.org/10.1109/MAP.2015.2437277.

Hansen, N., Müller, S.D., Koumoutsakos, P., 2003. Reducing the time complexity of the derandomized evolution strategy with covariance matrix adaptation. Evol. Comput. 11 (1), 1–18.

Hansen, N., Ostermeier, A., 2001. Completely derandomized self-adaptation in evolution strategies. Evol. Comput. 9 (2), 159–195.

Hickey, M.P., Schubert, G., Walterscheid, R.L., 1993. Gravity wave-driven fluctuations in the O2 atmospheric (0–1) nightglow from an extended, dissipative emission region. J. Geophys. Res. 98 (A8), 13717–13729.

Huang, T.-Y., George, R., 2014. Simulations of gravity wave-induced variations of the OH(8,3), O_2(0,1), and O(^{1}S) airglow emissions in the MLT region. J. Geophys. Res. Space Physics 119. https://doi.org/10.1002/2013JA019296.

Huang, T.-Y., 2015. Gravity waves-induced airglow temperature variations, phase relationships, and Krassovsky ratio for OH(8,3) airglow, O2(0,1) atmospheric band, and O(1S) greenline in the MLT region. J. Atmos. Sol. Terr. Phys. 130–131, 68. https://doi.org/10.1016/j.jastp.2015.05.002.

Huang, T.-Y., 2016. Simulations of airglow variations induced by the CO_2 increase and solar cycle variation from 1980 to 1991. J. Atmos. Sol. Terr. Phys. 147, 138–147. https://doi.org/10.1016/j.jastp.2016.07.014.

Huang, T.-Y., 2017. Influences of CO_2 increase, solar cycle variation, and geomagnetic activity on airglow from 1960 to 2015. J. Atmos. Sol. Terr. Phys. https://doi.org/10.1016/j.jastp.2017.06.008 (in press).

Lednyts'kyy, O., von Savigny, C., Eichmann, K.-U., Mlynczak, M.G., 2015. Atomic oxygen retrievals in the MLT region from SCIAMACHY nightglow limb measurements. Atmos. Meas. Tech. 8, 1021–1041. https://doi.org/10.5194/amt-8-1021-2015.

Liu, G., Shepherd, G., 2006. Perturbed profiles of oxygen nightglow emissions as observed by WINDII on UARS. J. Atmosp. Solar-Terrest. Phys. 68 (9), 1018–1028. https://doi.org/10.1016/j.jastp.2005.12.004, ISSN 1364-6826.

Lopez-Gonzalez, M.J., Lopez-Moreno, J.J., Rodrigo, R., 1992. Atomic oxygen concentration from airglow measurements of atomic and molecular oxygen emissions in the nightglow. Planet Space Sci. 40, 929–940.

McDade, I.C., Murtagh, D.P., Greer, R.G.H., Dickinson, P.H.G., Witt, G., Stegman, J., Llewellyn, E.J., Thomas, L., Jenkins, D.B., 1986. Eton 2: Quenching parameters for the proposed precursors of $O_2(b_g^{1+})$ and O(^{1}S) in the terrestrial nightglow. Planet. Space Sci. 34 (9), 789–800.

Medeiros, A.F., Takahashi, H., Buriti, R.A., Pinheiro, K.M., Gobbi, D., 2005. Atmospheric gravity wave propagation direction observed by airglow imaging in the South American sector. J. Atmosp. Solar-Terrest. Phys. 67, 1767–1773.

Melo, M.L., Takahashi, H., Clemesha, B.R., Batista, P.P., Simonich, D.M., 1996. Atomic oxygen concentrations from rocket airglow observations in the equatorial region. J. Atmos. Terr. Phys. 58 (16), 1935–1942.

Murtagh, D.P., Witt, G., Stegman, J., McDade, I.C., Llewellyn, E.J., Harris, F., Greer, R.G.H., 1990. An assessment of proposed O(^{1}S) and $O_2(b_g^{1+})$ nightglow excitation parameters. Planet. Space Sci. 38 (1), 43–53.

Ogawa, T., Iwagami, N., Nakamura, M., Takano, M., Tanage, H., Takechi, A., Miyashita, A., Suzuki, K., 1987. A simultaneous observation of the height profiles of the night airglow, OI 5577 Å, Herzberg and Atmospheric bands. J. Geomagn. Geoelect. 39, 211–228.

Picone, J.M., Hedin, A.E., Drob, D.P., Aikin, A.C., 2002. NRLMSISE-00 empirical model of the atmosphere: statistical comparisons and scientific issues. J. Geophys. Res. 107 (A12), 1468.

Russell, J.P., Lowe, R.P., 2003. Atomic oxygen profiles (82 to 96 km) derived from WINDII/UARS measurements of the Hydroxyl Airglow I: validation of technique. J. Geophys. Res. 108, 4662–4669.

Russell, J.P., Lowe, R.P., Ward, W.E., 2004. Atomic oxygen annual and semi-annual variations in the mesopause region for mid and equatorial latitudes. J. Atmos Sol. Terr. Phys. 66 (6–9), 451–461. https://doi.org/10.1016/j.jastp.2004.01.004.

Seakins, P.W., 2007. Product branching ratios in simple gas phase reactions. Annual Rep., Sect C, Phys. Chem. 103, 173–222.

Schubert, G., Walterscheid, R.L., Hickey, M.P., Tepley, C.A., 1999. Observations and interpretation of gravity wave induced fluctuations in the O I (557.7 nm) airglow. J. Geophys. Res. 104 (A7), 14915–14924. https://doi.org/10.1029/1999JA900096.

Shepherd, G.G. et al., 1993. WINDII, the wind imaging interferometer on the Upper Atmospheric Research Satellite. J. Geophys. Res. 98, 10725–10750.

Siskind, D.E., Sharp, W.E., 1991. A comparison of measurements of the oxygen nightglow and atomic oxygen in the lower thermosphere. Planet. Space Sci. 39, 627.

Snively, J.B., Pasko, V.P., Taylor, M.J., 2010. OH and OI airglow layer modulation by ducted short period gravity waves: effects of trapping altitude. J. Geophys. Res. 115, A11311. https://doi.org/10.12029/2009JA015236.

Solheim, B.H., Llewellyn, E.J., 1979. An indirect mechanism for the production of O(1S) in the aurora. Planet. Space Sci. 27, 473–479.

Stegman, J., Murtagh, D.P., 1991. The molecular oxygen band systems in the U.V. nightglow: measured and modelled, Planet. Space Sci. 39,595.

Takahashi, H., Clemesha, B.R., Simonich, D.M., Melo, S.M.L., Eras, A., Stegman, J., Witt, G., 1996. Rocket measurements in the equatorial airglow: MULTIFOT 92 database. J Atmos Terr Phys 58, 1943–1961.

Taylor, M.J., Bishop, M.B., Taylor, V., 1995. All-sky measurements of short period waves imaged in the OI(557.7 nm), Na(589.2 nm) and near infrared OH and O2(0,1) nightglow emissions during the ALOHA-93 campaign. Geophys. Res. Lett. 22, 2833–2836.

Vargas, F., Swenson, G.R., Liu, A.Z., 2015. Evidence of high frequency gravity wave forcing on the meridional residual circulation at the mesopause region. Adv. Space Res. 56, 1844–1853. https://doi.org/10.1016/j.asr.2015.07.040.

von Zahn, U., 1987. The project MAP/WINE: an overview. J. Atmosp. Solar-Terrest. Phys. 49 (7–8), 607–620. https://doi.org/10.1016/0021-9169(87)90007-9.

Witt, G., Stegman, J., Murtagh, D.P., McDade, I.C., Greer, R.G.H., Dickinson, P.H.G., Jenkins, D.B., 1984. Collisional energy transfer and the excitation of O2(b1) in the atmosphere. J. Photochem. 25, 365.